Catalysis Today 418 (2023) 114066

Contents lists available at ScienceDirect

Catalysis Today

journal homepage: www.elsevier.com/locate/cattod

Nitrogen-containing carbon nanofibers as supports for bimetallic Pt-Mn catalysts in aqueous phase reforming of ethylene glycol

Monica Pazos Urrea, Felix Herold, De Chen, Magnus Rønning *

Department of Chemical Engineering, Norwegian University of Science and Technology, 7491 Trondheim, Norway

ARTICLE INFO

Keywords:
Aqueous phase reforming
Carbon nanofibers
Nitrogen doping
Bimetallic catalyst

ABSTRACT

Aqueous phase reforming (APR) of ethylene glycol was performed at 225 °C and 30 bar in batch and continuous reaction conditions. The effect on the APR performance by functionalizing carbon supports with nitrogen and adding Mn to Pt-based catalysts was investigated. The presence of nitrogen species on the carbon surface and Mn-addition (PtMn) improved the catalytic activity and promoted H_2 production. XPS results suggest that the enhancement of the catalytic activity may be attributed to charge transfer from platinum to the nitrogen groups and Mn. Pt-based catalysts were stable under the studied reaction conditions, while up to 97 % of the manganese leached into the liquid solution during APR. However, the catalytic activity was maintained even with such significant decrease in Mn content, indicating that only a small amount of Mn is necessary to maintain the promotional effect on Pt during APR.

1. Introduction

Aqueous phase reforming (APR), a process proposed by Dumesic and co-workers, utilizes biomass-derived wastewater streams to produce H_2 at relatively mild reaction conditions [1]. The APR process offers favorable conditions to obtain a H_2-rich stream with low CO content through the water-gas shift reaction (WGS). However, side reactions are also promoted, such as methanation and Fisher-Tropsch synthesis reactions, leading to formation of undesirable alkanes.

Sustainable H_2-rich streams can be used for fuel cell applications, the production of ammonia and synthetic liquid fuels, aiding to mitigate the intermittent nature of renewable energy [2]. However, the activity and stability of the catalyst during APR are compromised by the hydrothermal conditions in the presence of oxygenates at 200–270 °C and 20–60 bars, leading to deactivation through sintering, coke deposition, metal phase oxidation, and metal leaching.

APR catalysts must withstand severe hydrothermal conditions and exhibit strong metal-support interactions to minimize catalyst deactivation. Thus, the nature of the catalyst support plays a key role in the catalytic APR performance. Oxide supports such as TiO_2, ZrO_2, MgO, Al_2O_3 and SiO_2 suffer pore degradation and phase transformation under hydrothermal conditions leading to catalyst deactivation [3–6]. Carbon materials, including carbon black, carbon nanotubes, carbon nanofibers and mesoporous carbons demonstrate their high hydrothermal stability, resistance to acidic media and tunable chemical properties when studied in APR [7–10]. Nonetheless, the broad distribution of pore sizes, high microporosity and irregular pore structure of some carbon materials limit their applicability for APR, influencing the diffusion of the reactants and products throughout the structure of the catalyst [11].

Carbon nanofibers (CNF) are suitable as support material for APR due to their unique structural and textural properties that can be tuned according to the synthesis conditions. Various ratios of edge/basal atoms in the carbon structure lead to different CNF structures [12]. Platelet carbon nanofibers have their graphite sheets stacked perpendicularly to the fiber axis, thus exposing predominantly carbon edge sites [13]. These edge sites can be used as anchoring sites for metal particles on the carbon support giving stronger metal-support interactions [12,14–16], a desirable feature to enhance catalyst stability at APR conditions.

Pt is the most studied metal for APR since it is highly active and selective towards hydrogen production [17]. However, it has been demonstrated that using bimetallic catalyst such as Pt-Ni [18] Pt-Re [19] Pt-Co [20] and Pt-Mn [11] promotes the catalytic activity. For example, Re and Co are known for favoring the WGS reaction by tuning the electronic properties of the catalyst and modifying the biding energies of CO [21,22]. However, base metals are affected by the hydrothermal conditions in APR. Van Haasterecht et al. [7] studied cobalt, nickel, copper and platinum supported on CNF in APR of ethylene glycol and observed leaching of the base metal catalyst due to oxidation in the

* Corresponding author.
E-mail address: magnus.ronning@ntnu.no (M. Rønning).

https://doi.org/10.1016/j.cattod.2023.114066
Received 31 October 2022; Received in revised form 21 February 2023; Accepted 26 February 2023
Available online 1 March 2023

acidic media. A similar pattern is observed for Mn where most of the metal leached out during APR [9].

Thus, to promote the interaction between the metal particles and the support, functionalization of the carbon surface is proposed as a promising route. It has previously been observed that nitrogen-doping of carbon supports has a positive effect in liquid phase reactions. It is shown to be advantageous for the distribution of meal particles on the support, enhance the metal-support interaction, as well as modifying the electronic structure of the metal particles [23–26]. Gogoi et al. [23] observed that the nitrogen on the support not only aids in anchoring of Ru particles on the surface but also decreases the reduction temperature of Ru nanoparticles. This decrease is attributed to interactions between electron-rich nitrogen atoms present on the carbon surface and the Ru species, leading to a higher fraction of metallic Ru during APR of glycerol.

In this work we evaluate the promoting effect of nitrogen surface functionalization of a platelet CNF support on Pt and Pt-Mn based catalyst by evaluating the catalytic activity, selectivity and stability in APR of ethylene glycol (EG). Mn, a known unstable promoter at APR conditions, was selected to evaluate if the surface modification of the support in addition to the interaction with Pt is sufficient to stabilize Mn during APR. The role played by the support and the properties introduced to stabilize the metals on the support are discussed.

2. Experimental section

2.1. Catalyst synthesis

2.1.1. Carbon nanofiber synthesis

The preparation of platelet carbon nanofibers (CNF) has been described in detail elsewhere [27]. In short, carbon nanofibers were synthetized by chemical vapor deposition in a tubular quartz reactor using a Fe_3O_4 catalyst. About 100 mg of catalyst was reduced in 25 % H_2/Ar (100 mL/min) at 600 °C for 6 h (heating rate 5 °C/min), followed by flushing with Ar for 30 min. A synthesis mixture of CO/H_2 (50/12.5 mL/min) was introduced to grow CNF at 600 °C for 46 h.

2.1.2. Functionalization of CNF

To remove the Fe_3O_4 CNF growth catalyst contained in the fibers and to introduce surface functional oxygen groups, the as-synthetized CNF were treated in concentrated nitric acid (70 %) under reflux conditions for 3 h at 90 °C. Subsequently, the suspension was filtered, washed with deionized water until pH 7 was reached, and dried overnight at 100 °C. The acid treated CNF are denoted CNF-ox.

Heat treatment of CNF-ox was carried out in a quartz reactor inside a vertical tubular furnace. The CNF-ox were subjected to heat treatment in argon (100 mL/min) for 2 h at 700 °C to remove unstable oxygen groups introduced to the carbon surface during the acid treatment. The heat-treated CNF are denoted CNF-HT.

A gasification-assisted heteroatom doping method was utilized for nitrogen-doping of CNF-ox (N-CNF). The method consists of generating defects on the carbon surface with the aid of a gasification agent (H_2O) in the presence of a gaseous nitrogen source at high temperature. Nitrogen will occupy the new sites created by the gasification of carbon.

A vertical tubular furnace with a quartz reactor was used for the N-doping with ethylene diamine as the nitrogen source. First, 365 mg of CNF-ox were loaded into the reactor and heated to 875 °C at a heating rate of 10 °C/min in N_2 atmosphere (200 mL/min). Once the system reached the desired temperature, the nitrogen stream was saturated by flowing through a sparger with 1:1.5 (mol: mol) ethylene diamine/water solution and fed into the reactor for 90 min. Then, the system was cooled down in N_2 atmosphere (100 mL/min). A schematic drawing of the experimental setup is provided in Fig. S1.

2.1.3. Catalyst synthesis

Platinum (nominal loading 3 %wt) was introduced to the CNF by incipient wetness impregnation using chloroplatinic acid hexahydrate H_2PtCl_6 x6H_2O (Sigma-Aldrich, > 37 % Pt basis) as metal precursor and acetone (Sigma Aldrich, 99.9 %) as solvent. The support material was mixed dropwise with the Pt solution and kept at room temperature overnight, followed by drying at 100 °C for 20 h. Subsequently, the prepared catalyst was heat-treated in N_2 atmosphere (100 mL/min) at 320 °C (heating rate 3 °C/min) for 2 h to decompose the precursors from the synthesis.

A similar procedure was followed for the bimetallic Pt-Mn catalysts using manganese (II) nitrate hydrate $Mn(NO_3)_2{\cdot}xH_2O$ (Sigma Aldrich, 98 %) as Mn precursor and acetone as solvent. Pt and Mn solutions were added to the CNF support by co-impregnation (nominal loading 3 %wt and 0.8 %wt), followed by drying and decomposition using the same conditions as for the monometallic catalysts.

2.2. Catalyst characterization

Textural properties of the carbon supports were measured by N_2 physisorption at − 196 °C using a Micromeritics Tristar 3000 instrument. About 100 mg of the samples were degassed overnight at 200 °C prior the analysis. The specific surface area was calculated by the BET method [28].

CO chemisorption was carried out in a Micromeritics ASAP 2020 instrument. 100 mg of the sample was reduced *in situ* for 1 h in pure H_2 at 300 °C with a heating rate of 5 °C/min. After the reduction, the system was purged in helium at 120 °C for 30 min before cooling down to 35 °C for the chemisorption analysis. Pt dispersion was evaluated assuming a Pt/CO adsorption stoichiometry of 1 [29]. The error in the chemisorption measurements is obtained from repeated measurements assumed to be in the range of 1–2.5 %, giving a standard deviation in the dispersion values of + /- 1.

The particle size (d) in nm was estimated assuming spherical shape from Eq. (1).

$$D = \frac{6M}{\rho d N_a S_a} \tag{1}$$

Where D is the metal dispersion (%) obtained by CO chemisorption, M is the atomic weight, N_a is Avogadro's number, S_a the area of each surface atom and $\rho$the density of Pt ($21.45 g/cm^3$).

X-ray diffraction was carried out in a Bruker D8 A25 DaVinci X-ray diffractometer using Cu Kα radiation and a LynxEye detector. Diffractograms were acquired in the 2θ range 10–80° with a step size of 0.044°. Peak identification was conducted by comparing it to the crystallography open database [30]. The Scherrer equation was used to estimate the Pt average crystallite size from the XRD pattern. The Scherrer constant d was assumed as 0.89 [31].

Metal loading was determined by microwave plasma atomic emission spectroscopy (Agilent 4210 MP-AES optical emission spectrometer). The samples were prepared by microwave assisted digestion using a speedwave XPERT (Berghof) instrument. The digestion was carried out in two steps, initially heating up to 170 °C, remaining at this temperature for 10 min followed by an increase in temperature to 210 °C for 20 min with a power of 2 × 800 W in 10 mL HCl/HNO_3 mixture (1:4, vol:vol). Then, the samples were transferred to a 100 mL volumetric flask, adjusting the volume with Millipore Milli-Q water, and filtered with a syringe filter (0.2 μm) before the analysis. External calibration with Pt and Mn standards for ICP (Sigma-Aldrich, 1000 mg/L) was carried out before every measurement.

X-ray photoelectron spectroscopy (XPS) was performed at ambient temperature under ultra-high vacuum (UHV). The measurements were conducted in a Kratos Analytical Axis Ultra DLD spectrometer using monochromatic Al Kα radiation (1486.6 eV) operating the anode at 10 kV with an aperture of 700 × 300 μm. For each sample, a survey spectrum was measured with a pass energy of 160 eV, while high-resolution spectra were recorded with a pass energy of 20 eV. The

binding energy scale of the system was calibrated to the C1s contribution of sp^2 carbon at 284.6 eV. The peaks were deconvoluted after Shirley background subtraction [32] and fitted to linear combinations of Gaussian and Lorentzian functions. The full set of band assignments as well as fitting parameters are listed in Table S1.

Samples for scanning transmission electron microscopy (STEM) were prepared by ultrasonic dispersion in n-hexane followed by drop-casting on carbon coated copper grids. STEM micrographs were obtained on a Hitachi SU9000 electron microscope operating at an accelerating voltage of 30 kV. Energy-dispersive X-ray spectroscopy (EDS) was performed at an accelerating voltage of 30 kV using an Oxford Ultim Extreme 100 mm^2 windowless detector.

2.3. Catalytic testing in aqueous phase reforming

2.3.1. Batch reactor testing

Aqueous phase reforming of ethylene glycol was carried out in a 160 mL stainless-steel mini bench reactor (Parr 4592 model) equipped with a magnetic driver stirrer and PID temperature controller (Parr Instruments Co., USA). A quartz reactor was employed for the *ex-situ* catalyst reduction in a vertical tubular furnace. Typically, the catalyst was reduced *ex-situ* at 300 °C for 1 h in 5 % H_2/N_2 flow (100 mL/min, heating rate 5 °C/min).

The pre-reduced catalyst (200 mg) and 30 mL of 6 %wt aqueous ethylene glycol solution were loaded into the vessel. The reactor was thoroughly purged with nitrogen and pressurized to an initial pressure of 20 bar, which served as an internal standard for the final quantification of the products present in the gas phase. The mixture was subsequently stirred at 500 rpm and heated to 225 °C. After 2 h at 225 °C, the reactor was quenched to room temperature in an ice water bath. Gaseous products were collected in a multilayer foil gas sampling bag (Supelco). After depressurization, the liquid products were collected and filtered with a 0.2 μm PTFE filter. The spent catalyst was recovered by filtration, washed with DI water, and dried overnight at 60 °C.

Gas phase products were analyzed by gas chromatography (Agilent 7820 A) equipped with a thermal conductivity detector (TCD) and a flame ionization detector (FID). H_2, CO, CO_2, N_2 and CH_4 were detected by TCD using a Porapak-Q GS-Q and CP-Molsieve 5 Å columns. Hydrocarbons were detected by the FID detector using a HP-Plot Al_2O_3 KCl column.

The liquid phase was analyzed by high-performance liquid chromatography (1260 Infinity II LC System, Agilent technologies) equipped with a refractive index detector. The separation of the products was carried out in an Agilent Hi-Plex H ion exclusion column (300 mm × 7.7 mm) with diluted sulfuric acid (5 mM) as the mobile phase at a flow rate of 0.6 mL/min and a temperature of 60 °C. External standard calibration with all foreseen reaction products was used.

The equations applied to evaluate the catalyst performance during aqueous phase reforming in batch conditions are shown in Table S2.

2.3.2. Continuous reactor testing

Aqueous phase reforming of ethylene glycol was conducted in continuous flow in a stainless-steel tubular reactor (internal diameter =15 mm; length = 385 mm). About 0.3 g of catalyst was sieved (125–250 μm) diluted with SiC (125–250 μm, 1:1 dilution in weight) and held in place with a stainless-steel frit and quartz wool plugs. Before the reaction, the catalyst was reduced *in situ* at 300 °C (heating rate 5 °C/min) in 10 % H_2/N_2 flow (100 mL/min) for 1 h. Then, N_2 was used to pressurize the system to 30 bars, and to regulate the pressure at a flow of 25 mL/min using a back pressure regulator. A 6 wt% ethylene glycol solution was introduced at 0.17 mL/min (2.0 h^{-1} weight hourly space velocity WHSV) in an up-flow configuration. The reaction was carried out at 225 °C. The evolution of the reaction products was monitored by an on-line gas chromatograph (Agilent 8890) equipped with a thermal conductivity detector (TCD) and a flame ionization detector (FID) using CP-Sil 5 CB, CP-Molsieve 5 Å and Haysep-A columns for separation of the components. Samples of the liquid phase were taken every hour and analyzed by an offline HPLC (described in Section 2.3.1). A schematic diagram of the experimental setup is provided in Fig. S2.

The equations used to quantify the catalyst performance during continuous operation are summarized in Table S3.

3. Results and discussion

3.1. Catalyst characterization

Textural characterization of the CNF was carried out to observe the differences in the CNF subjected to various surface treatments. The surface morphology of the as-synthesized catalysts is presented in Fig. S3, indicating the graphite layered structure perpendicular to the fiber axis, typical of platelet carbon nanofibers. The BET specific surface areas are summarized in Table 1, including carbon, oxygen and nitrogen content determined by XPS (at%).

The carbon supports are mainly mesoporous, with only minor differences in surface area. The oxidized carbon nanofibers (CNF-ox) show a higher surface area that decreases with the subsequent heat treatment or nitrogen functionalization of the carbon support. The most notable variation is a 15 % decrease in surface area after nitrogen functionalization of the carbon nanofibers.

The chemical composition and Pt dispersion of the synthesized catalysts are presented in Table 2. For the monometallic samples, Pt dispersion is relatively high and comparable for the different CNF supports. Similar results can be observed for the bimetallic samples, although introducing Mn lower the CO uptake of the catalyst, which is reflected in the values of dispersion. A possible explanation is that this lower CO uptake is a result of a physical blockage, where Mn covers the platinum atoms, as it was suggested by Jain et al. [33].

The XRD patterns of the catalysts are presented in Fig. 1. All samples showed the characteristic high-intensity graphite (002) peak at $2\theta = 26.2°$, which is associated with the graphitic structure of the carbon nanofibers (Fig. S5). Characteristic diffraction peaks of the Pt fcc structure were mainly observed in the catalyst with CNF-ox as support. No Pt diffraction peaks were detected in the N-CNF samples, indicating that the nanoparticles are well dispersed on this support.

From the STEM images (Fig. 2) a bimodal particle size distribution can be seen for the catalysts supported on CNF-HT. A large fraction of the Pt is finely dispersed on the surface, but a significant fraction of larger particles can also be observed in the images. The bimodal particle size distribution can be related to the discrepancy observed in the estimation of average crystallite size from XRD and chemisorption, which can be explained by the size detection limit of XRD. Only the large particles are detected by XRD, whereas the finely dispersed Pt fraction leads to relatively high dispersion values (35–50 %).

These observations indicate that the deposition of Pt by impregnation is affected by the surface functionalization of the carbon support, leading to larger aggregation of Pt nanoparticles when there is a high content of surface oxygen groups.

Several reports [10,34,35] have suggested that electrostatic interaction between the metal precursor and the heteroatoms present on the carbon surface have an effect on the dispersion of the nanoparticles during preparation of the catalyst. For impregnation, it is reported that oxygen-containing groups on the surface can be used as anchoring sites for the metal particles, preventing aggregation. However, when using an

Table 1
Textural properties and elemental composition of the functionalized CNF.

Support	BET surface area (m^2/g)	C (at%)	O (at%)	N (at%)
CNF	197	-	-	-
CNF-ox	209	95.0	5.0	-
CNF-HT	195	96.4	3.5	-
N-CNF	174	96.4	1.7	1.9

Table 2
Pt dispersion, metal loading and average particle size determined by CO chemisorption, MP-AES and XRD.

Catalyst	CO uptake (μmol g^{-1})[a]	Pt dispersion (+/- 1)[a]	Metal loading (±0.1 %)[b]		Pt particle size (nm)[a]	Crystallite size (nm)[c]
			Pt	Mn		
Pt CNF-ox	48.5	39	2.9		3	27
Pt CNF-HT	72.4	50	2.8	-	2	7
Pt N-CNF	52.1	40	2.5	-	3	-
PtMn CNF-ox	47.3	37	2.9	0.8	3	22
PtMn CNF-HT	45.9	34	2.6	0.8	3	16
PtMn N-CNF	46.0	35	2.6	0.8	3	-

[a] CO chemisorption.
[b] MP-AES.
[c] XRD using the Scherrer equation.

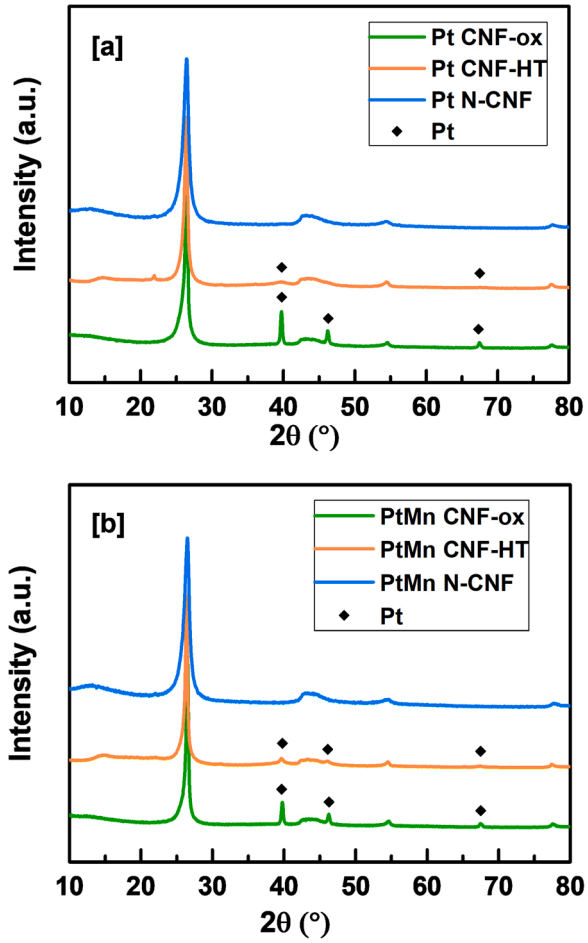

Fig. 1. [a] XRD patterns of monometallic catalysts (Pt). [b] XRD patterns of bimetallic catalysts (PtMn) supported on CNF-ox, CNF-HT, and N-CNF. The diffraction peaks of Pt metal are indicated in the figure.

anionic precursor such as $Pt(Cl_6)^{-2}$, the negatively charged ions could be repelled from the surface by acidic oxygen functional groups (such as carboxylic acids), favoring aggregation of Pt particles [10]. Thus, the formation of larger particles can be facilitated in CNF-ox and CNF-HT during impregnation. And it is suggested that the aggregation of the particles increases with the amount of oxygen content on the carbon surface, observing larger particles for the CNF-ox catalyst with 1.5 %at more oxygen than CNF-HT.

Detailed XPS characterization of the N-doped sample allowed for determination of the nitrogen species on the carbon surface. The XPS of the N-CNF support in the N 1 s region (Fig. 3[a]) indicates the presence of oxidized nitrogen species (402.7 eV), quaternary nitrogen species (401 eV), pyrrolic nitrogen (399.5 eV) and pyridinic nitrogen (398.4 eV) [36], in which the pyridinic functional groups were found to be the most abundant species on the surface (41.8 %). The concentration of individual nitrogen species on the surface of the catalyst is summarized in Table S4. Pyridinic nitrogen is known to be an electron acceptor when it is located on carbon vacancy sites [37,38]. It has been suggested that this nitrogen species have a strong donor-acceptor interaction with Pt nanoparticles by decreasing the electron density of Pt [39].

The N 1 s spectrum of Pt N-CNF (Fig. 3 [b]) shows a decrease in the fraction of pyridinic nitrogen groups (12.6 %) as well as an apparent drop in the overall N content (from 1.9 at% in N-CNF to 1.5 at% in Pt N-CNF) on the surface of the catalyst after deposition of Pt on the support. The loss in N content and specifically that of pyridinic N can be attributed to a preferential anchoring of the Pt nanoparticles on these sites, as has been observed in previous studies for other metals [40,41]. For the bimetallic catalyst (PtMn N-CNF in Fig. 3[c]), it is observed that the fraction of pyridinic nitrogen does not change significantly (44 %), while the overall N content drops from 1.9 %at for N-CNF to 1.4 %at for PtMn N-CNF. This finding indicates that Mn might not be selectively deposited on the pyridinic sites but randomly on all the functional N sites of the carbon.

XPS measurements were carried out to investigate the chemical valence of the Pt phase. The analysis was performed on the reduced catalysts before and after APR. This means that the catalysts were exposed to air when transported to the XPS chamber. The Pt in the catalysts is however still predominantly in the reduced state (*ca.* 80 %, see Table 3). It is thus assumed that the state of Pt in the catalysts is representative for the active state during reaction.

The binding energy of Pt species in the reduced samples is summarized in Table 3 and Fig. 4. From the deconvolution of the Pt regional spectra (Fig. S6), no apparent shift of the binding energy of Pt is observed when comparing Pt N-CNF with Pt CNF-HT. These results indicate that there is no change of the Pt electronic state due to the presence of nitrogen groups on the carbon surface. Previously, it has been observed that the typical binding energy of metallic platinum at Pt 4 $f_{7/2}$ (71.1 eV) is exceeded when platinum is supported on N-containing carbon, and that the Pt binding energy increases with higher content of N groups on the carbon surface [24,42]. Podyacheva et al. [41] reported a shift in Pt binding energies to 72 eV and 72.4 eV for Pt supported on carbon containing 3 at% and 7.5 at% of N, respectively. In this context, electron-withdrawing nitrogen species on the CNF surface may explain an increase in the Pt binding energy by withdrawing electrons from Pt, leading to a decrease in the electron density on the Pt particles. As a result, the Pt nanoparticles are stabilized by strong metal-support interactions leading to higher catalytic activity compared to Pt supported on non-doped carbons [15,34,43]. For the monometallic catalyst in this study, the nitrogen content is most likely too low (1.9 at%) to give a significant effect on the electronic density of Pt. However, a higher Pt^0/Pt^{2+} ratio can be observed for both catalysts supported on N-CNF, suggesting that the presence of nitrogen in the support increases the degree of reduction of Pt metal particles, as was observed for Ru catalysts studied by Gogoi et al. [23].

From Fig. 4 it can be seen that the bimetallic catalysts PtMn CNF-HT and PtMn N-CNF present a shift to higher binding energies for the Pt species. However, the most significant effect is observed in the bimetallic catalyst supported on N-doped CNF, with a shift of approximately 1.5 eV compared to Pt CNF-HT. These results indicate that not only the

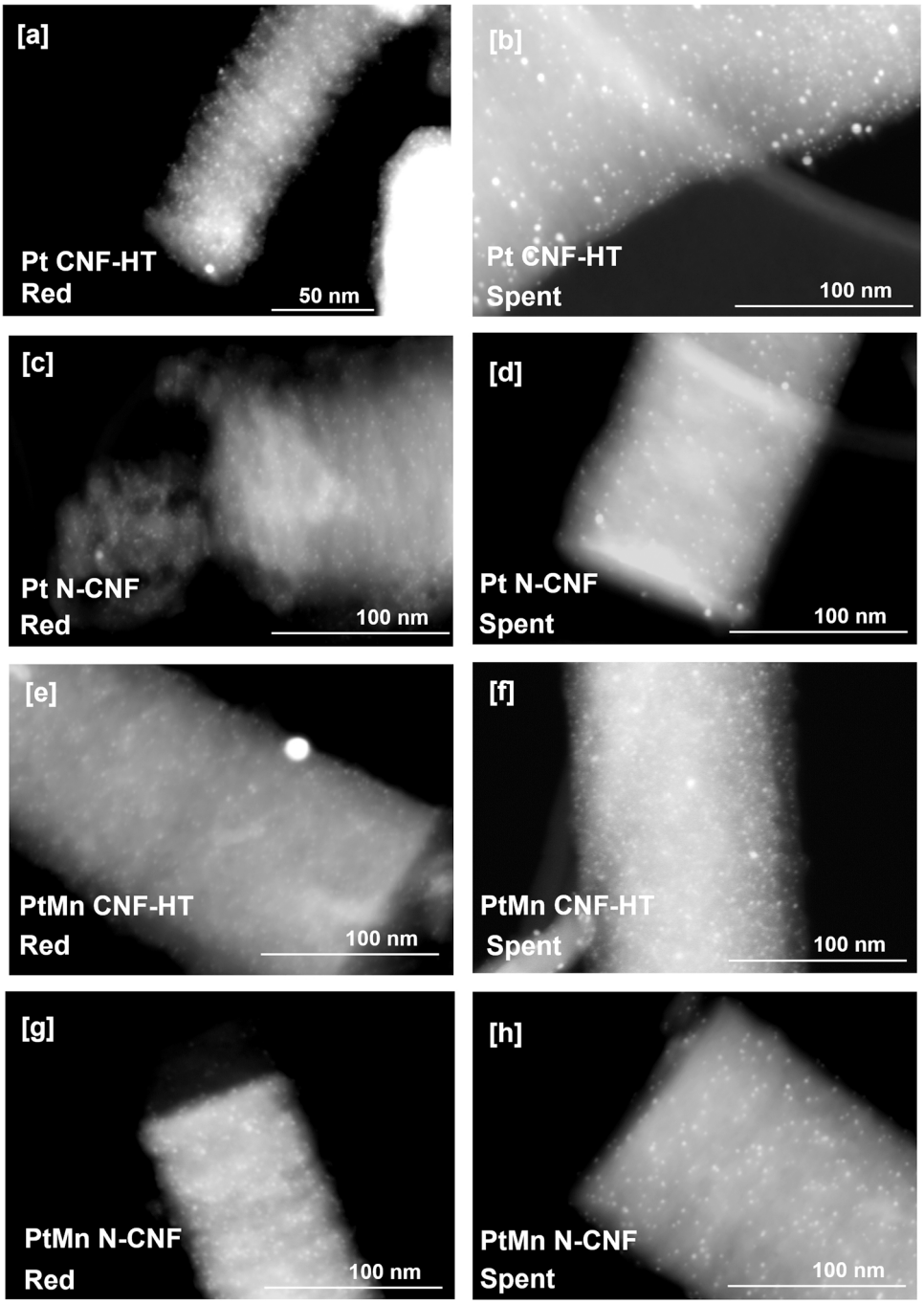

Fig. 2. STEM images of the reduced and spent catalysts after APR of ethylene glycol for 20 h at 225 °C, 30 bar. [a] Pt CNF-HT reduced [b] Pt CNF-HT spent [c] Pt N-CNF reduced [d] Pt N-CNF spent [e] PtMn CNF-HT reduced [f] PtMn CNF-HT spent [g] PtMn N-CNF reduced [h] PtMn N-CNF spent. Note that the scale bar is 50 nm for Fig. 4 [a] and 100 nm for all the other images.

presence of Mn affects the electronic state of Pt [44], but also nitrogen groups present on the surface of the carbon support are further decreasing the electron density on Pt.

Evaluating heat-treated PtMn CNF-HT with no nitrogen groups on the CNF surface and nitrogen-containing PtMn N-CNF allowed to distinguish sources of binding energy shifts in the Pt 4 f region spectra. PtMn CNF-HT shows a shift of 0.8 eV to higher binding energies compared to Pt CNF-HT, which can be attributed to the presence of oxidized Mn species. The XPS Pt 4 f spectrum of PtMn N-CNF shows the combined influence of the presence of Mn as well as electron withdrawing nitrogen groups on the carbon supports, which amounts to an overall shift of 1.5 eV.

In addition, XPS measurements of Mn $2p_{3/2}$ spectra suggested that Mn should be predominantly in oxidized state, although these results must be interpreted with cation due to the low signal to noise ratio (Fig. S7). The presence of oxidize manganese is consistent with earlier observations from Bossola et al. [9], attributing the activation of glycerol in reforming reactions to strong Lewis sites formed by $Mn^{\delta+}$ oxide, leading to higher H_2 production rates.

3.2. APR of ethylene glycol in batch reactor

Screening of the catalysts in APR of 6 %wt ethylene glycol solution at 225 °C was carried out in a batch reactor with an initial pressure of

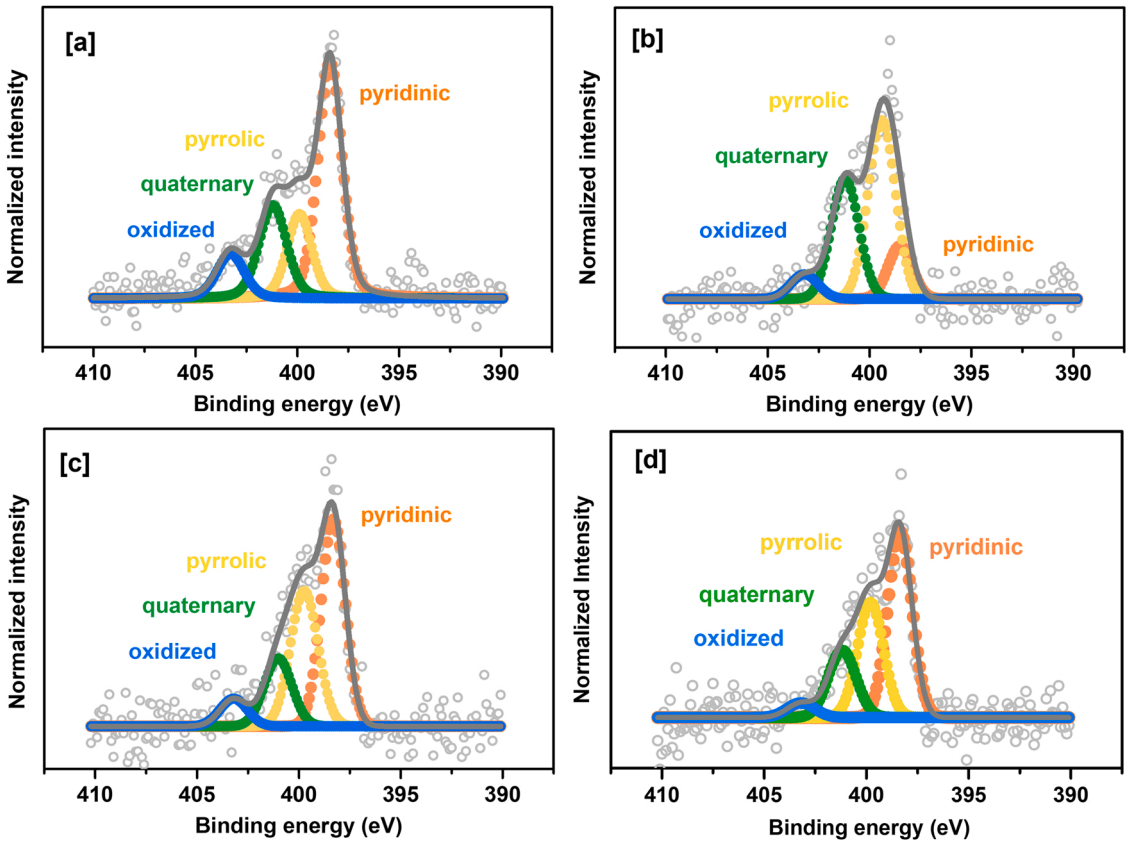

Fig. 3. N1s spectra of [a] N-CNF (1.9 at% nitrogen content) [b] Pt N-CNF (1.5 at% nitrogen content) [c] PtMn N-CNF (1.4 at% nitrogen content) [d] Spent PtMn N-CNF after APR (1.2 at% nitrogen content).

Table 3
Pt 4f7/2 binding energies of Pt species and fractions of Pt species for the reduced catalysts Pt CNF-HT, Pt N-CNF, PtMn CNF-HT, PtMn N-CNF.

	Pt^0 (4 $f_{7/2}$) Binding energy [eV]	Pt^{2+} (4 $f_{7/2}$) Binding energy [eV]	Pt^0 Fraction (+/- 0.01)	Pt^{2+} Fraction (+/- 0.01)	Pt^0/ Pt^{2+} ratio
Pt CNF-HT	70.90	72.68	0.79	0.21	3.8
Pt N-CNF	70.95	72.79	0.82	0.18	4.9
PtMn CNF-HT	71.71	73.20	0.74	0.26	3.2
PtMn N-CNF	72.42	74.18	0.82	0.18	4.9
PtMn CNF-HT spent	72.04	73.99	0.80	0.20	4.0
PtMn N-CNF spent	71.99	73.67	0.77	0.23	3.3

20 bar. Control experiments with CNF-ox, CNF-HT, and N-CNF presented negligible conversion of EG, indicating that the remaining growth catalyst (Fe_3O_4) in the carbon structure (Fe content 0.02–0.1 % wt) did not influence the APR experiments.

The catalytic activity and carbon yield to liquid products of the Pt and PtMn catalysts on the functionalized CNF supports are presented in Figs. 5 and 6. The main products in the gas phase were H_2, CO_2 and CH_4, whereas methanol, ethanol, acetic acid and glycolic acid dominated in the liquid phase. The monometallic samples do not show significant difference in activity and selectivity towards H_2 production for the various surface functionalization of the CNF. A common trend among the catalysts is high H_2 selectivity (>80 %) and low alkane formation (<5 %). The production of acetic acid is suppressed in the presence of N groups on the support. Small organic acids, such as acetic acid, are produced by the rearrangement of glycolic aldehyde, an intermediate product produced by the dehydrogenation of ethylene glycol [1,7]. Thus, it is likely that dehydrogenation of ethylene glycol is less favorable in the presence of N groups on the carbon surface.

In terms of catalytic activity of the monometallic catalysts, van Haasterecht et al. [7] have shown that Pt supported on CNF shows a higher ethylene glycol conversion than Pt supported on alumina in aqueous phase reforming. In addition, it has been demonstrated that the interaction between Pt and CNF results in a positive effect on the catalytic performance of several reactions [15,34,45]. Chen et al. [15] observed a higher Pt binding energy when supported on platelet CNF compared to other carbon supports, attributing the catalytic performance in ammonia borane hydrolysis to electron-deficient Pt particles. In APR, the change in the electronic properties of Pt nanoparticles could decrease the heat of absorption of CO and H_2, which are commonly strongly adsorbed species that block the active sites, thus having more available sites for ethylene glycol conversion [21].

The promoting effect of the N-doping can be clearly observed in the bimetallic samples, with high H_2 selectivity (85.8 %) and H_2 site time yield (22 min^{-1}) obtained for the N-doped catalyst (Table S5). As the mean particle size for all samples is comparable, the effect of nitrogen-doping of the carbon support could be confirmed.

Several lines of observations in previous literature suggest possible reasons for the improved catalytic activity of Pt supported on N-doped carbon. Nitrogen groups on the carbon surface could enable strong metal-support interactions by charge transfer from Pt to the nitrogen groups, as has been observed for pyridinic N [46]. Additional active sites may be formed on the metal-support interface by creating additional

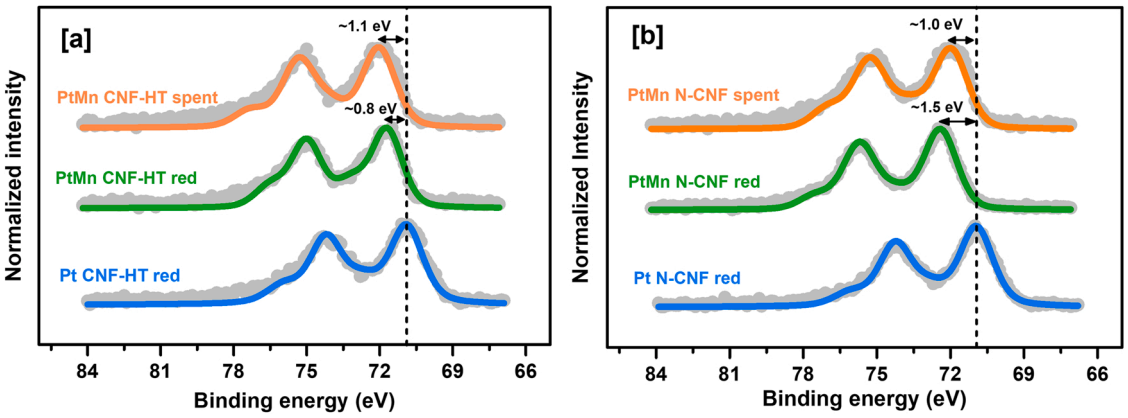

Fig. 4. Pt 4 $f_{7/2}$ spectra of [a] Pt CNF-HT, PtMn CNF-HT catalysts after reduction ex situ and spent PtMn CNF-HT after APR [b] Pt N-CNF, and PtMn N-CNF catalysts after reduction ex situ and spent PtMn N-CNF-HT after APR.

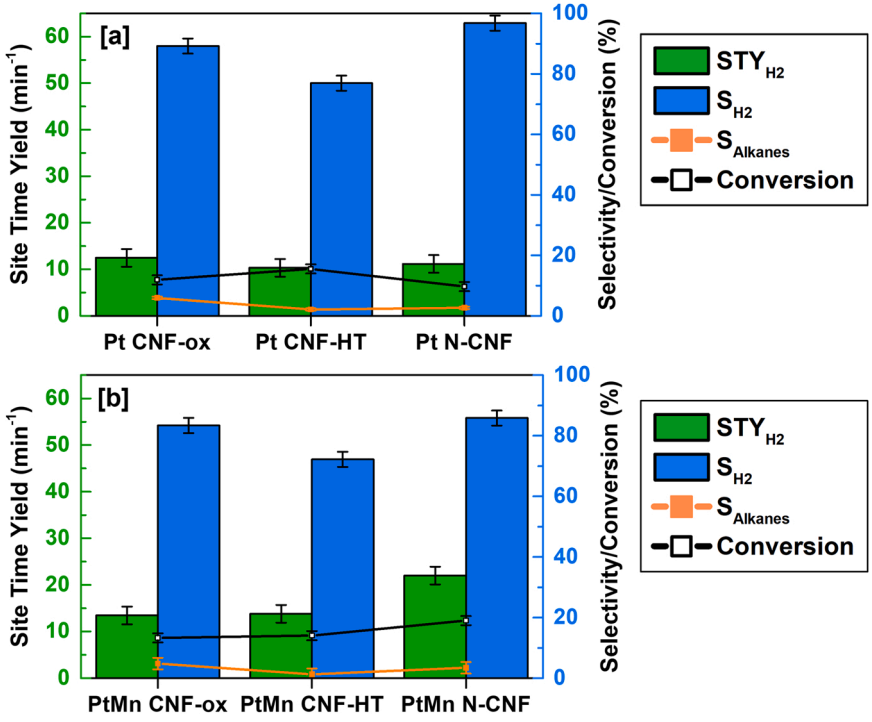

Fig. 5. APR of 6 %wt ethylene glycol (EG) aqueous solution at 225 °C and 20 bar initial pressure obtained in batch reactor. Catalytic conversion of EG, H_2 site time yield ($STYH_2$), H_2 and alkane selectivities for the [a] monometallic Pt catalysts. [b] bimetallic PtMn catalysts. The error bars represent the standard deviation of the experiments.

defects on the carbon surface by incorporation of nitrogen in the carbon structure [41]. N-doped carbon facilitates high dispersion and stability of the metal nanoparticles on the support, with N surface groups acting as anchoring sites for the nanoparticles on the carbon [39,41,47].

In this study, enhancement of the catalytic activity can not only be attributed to the surface functional groups on the carbon support. The addition of Mn promotes the formation of H_2, resulting in higher H_2 site time yield when compared to the monometallic catalyst. From the STEM-EDX maps of our catalyst (Fig. S8), a homogenous distribution of the two metals in on the surface can be observed, suggesting direct interaction between the two metals. As noted by Kim et al., [11] alloy formation between Pt and Mn may be responsible for enhancement of the catalytic activity, increasing H_2 selectivity and improving the stability of the catalyst. In the present study the electronic interaction between PtMn and the N groups contained on the surface of the CNF was confirmed by the XPS analysis (Table 2). Hence, the higher catalytic activity of PtMn N-CNF can be attributed to electron-deficient Pt present on the surface of the CNF.

Harsh hydrothermal conditions are characteristic of aqueous phase reforming and lead to the formation of organic acids in the liquid phase, which lowers the pH of the solution from nearly neutral to pH 3–4. Such conditions increase the risk of metal leaching by oxidation of the active metal phase. Metal leaching of the catalysts was examined by comparing the metal loading of the spent catalysts with the freshly reduced samples. For the bimetallic catalysts, a significant loss of Mn was observed (Table 4). Between 95 % and 97 % of the Mn was lost during 2 h of APR, demonstrating that the functionalization of the carbon support was not sufficient to stabilize the Mn species. However, for both bimetallic and monometallic catalysts, Pt nanoparticles were stable with no significant leaching (<1 %).

Due to the high degree of Mn leaching, the accumulation of soluble Mn species in the reaction media during batch operation may influence

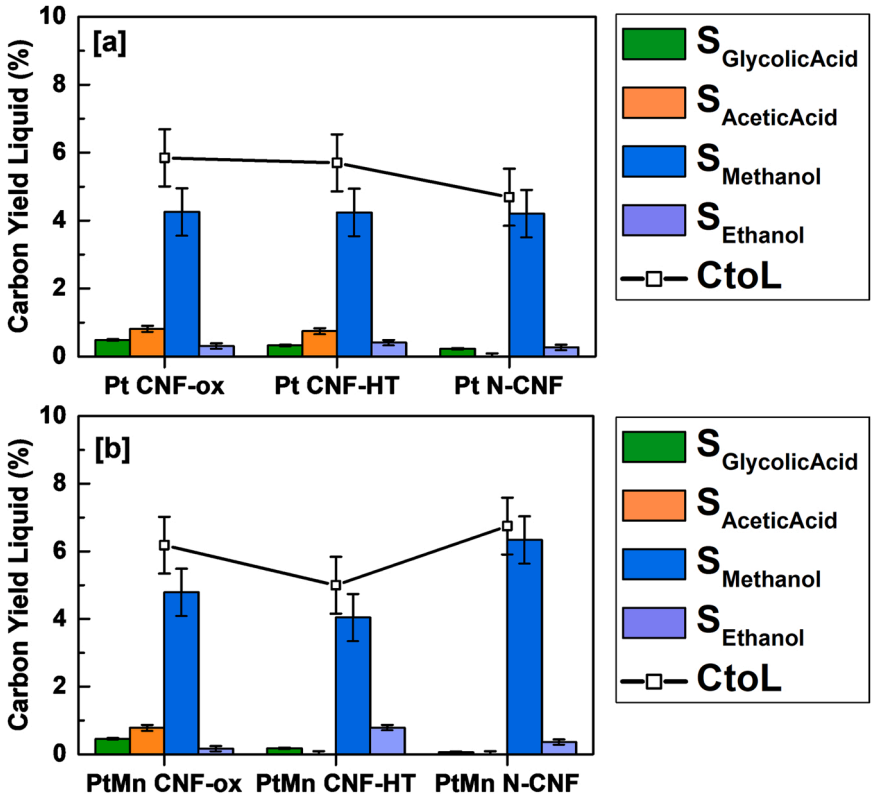

Fig. 6. APR in batch reactor of 6 %wt ethylene glycol (EG) aqueous solution at 225 °C and 20 bar initial pressure. Carbon yield to main liquid products and total conversion of carbon to liquids (CtoL) of the [a] monometallic Pt catalysts [b] bimetallic PtMn catalysts. The error bars represent the standard deviation of the experiments.

Table 4
Metal leaching of the spent catalyst determined by MP-AES.

Catalyst	Metal leaching (±0.1 %)	
	Pt	Mn
Pt CNF-ox	1.0	
Pt CNF-HT	0.0	-
Pt N-CNF	0.0	-
PtMn CNF-ox	0.3	96.3
PtMn CNF-HT	0.0	97.6
PtMn N-CNF	0.0	95.6

the outcome of the APR of EG. Therefore, a control experiment containing soluble Mn species ($Mn(NO_3)_2$ x H_2O) representing the total amount of Mn contained in the catalysts (~ 400 ppm) was carried out. No discernible conversion of ethylene glycol was detected in the batch experiment with the soluble Mn species.

Previous studies on aqueous phase reforming have reported high degrees of metal leaching from the catalyst matrix in similar systems (Pt-Ni, Pt-Mn, Pt-Co) [7,9,18,48]. In some cases, it has been demonstrated that although more that 50 % of the secondary metal is leaching out from the catalyst, the catalyst maintained the activity [49].

3.3. APR of ethylene glycol in continuous flow conditions

It is challenging to evaluate the stability of the catalysts in batch reaction. Accumulation of the products during reaction may favor conditions for deactivation of the catalyst, such as lower pH that can induce leaching of the active phase. Thus, the most active catalysts from the batch tests were studied in a continuous APR setup to further study the catalytic activity and stability. In the limiting case of the highest reaction rate the Weisz-Prater criterion was evaluated to confirm absence of intraparticle mass-transfer limitations (see SI).

Fig. 7 shows the catalytic activity of the catalysts supported on CNF-HT and N-CNF during time on stream expressed by EG conversion, H_2 site time yield (STY), methane selectivity and carbon yield. The reaction conditions were maintained for at least 20 h to reach steady-state performance. As can be seen from conversion and STY_{H2}, the catalyst reached steady-state after approximately 15 h of time on stream.

The main products in the gas phase during APR of ethylene glycol are H_2, CO_2, CO, methane, and ethane. Higher hydrocarbons were not detected in the GC analysis during continuous flow operation. From the gas phase selectivities (Table S6), it can be seen that all samples follow a general trend with low concentrations of CO and methane that decrease with time on stream. The STY_{H2} of all catalysts increased with TOS until reaching steady-state, except for the bimetallic catalyst supported on N-doped carbon which even after 20 h of reaction showed increasing production of hydrogen, which can be associated to lower rates on side-reactions consuming H_2, such as methanation and Fischer–Tropsch synthesis. The catalysts supported on nitrogen-doped CNF showed high H_2 selectivity (90 %), with the highest H_2 selectivity measured for the bimetallic PtMn N-CNF catalyst (96 %).

After 20 h of reaction, the most active catalysts are the PtMn-based catalysts, in which PtMn N-CNF displays the highest H_2 site time yield (15.8 min^{-1}) with the lowest production of alkanes among the catalysts. These results are in agreement with comparable studies where Pt-based catalysts are investigated. Huber et al. [21] studied the effects of addition of a second metal to Pd and Pt-based catalysts supported on alumina: They noticed that most of the bimetallic catalysts (PtNi, PtCo, PtFe) displayed higher turnover frequencies for H_2 production than the monometallic counterparts in aqueous phase reforming of ethylene glycol, showing TOF_{H2} values in the range 7–11 min^{-1}. Bossola et al. [9] studied aqueous phase reforming of glycerol over Pt and PtMn catalysts supported on carbon with TOF_{H2} values between 13 and 17 min^{-1}.

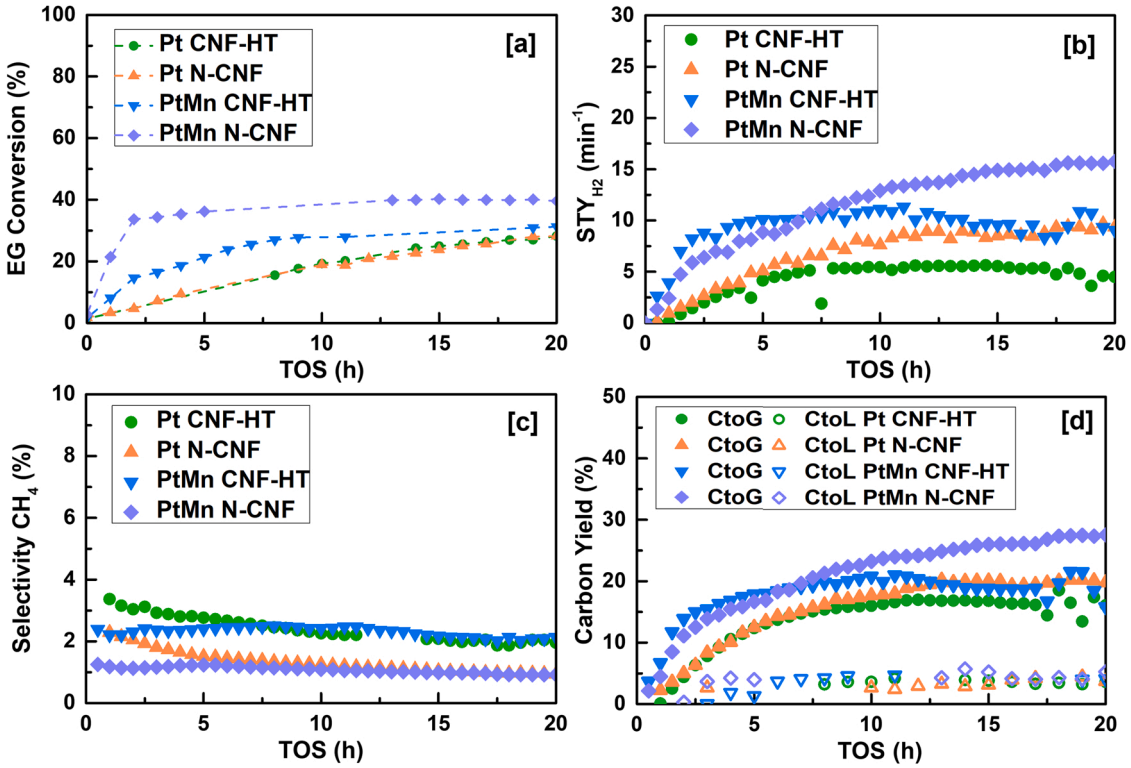

Fig. 7. APR of ethylene glycol (6 %wt) at 225 °C, 30 bar and WHSV= 2 h^{-1}. Evolution of [a] Ethylene glycol conversion (%) [b] H_2 site time yield (min^{-1}) [c] Selectivity to CH_4 [d] Carbon yield to liquid phase and gas phase (%) with time on stream (TOS).

Hence, the observed catalytic activity presented in Fig. 7 is in line with previous observations reported in literature.

The selectivity towards liquid phase products is comparable for the tested catalysts. Organic acids mainly produced during APR by ethylene glycol dehydrogenation followed by molecular rearrangement, such as organic acids [50] are not detected, in contrast to the results from the batch reactor. Methanol and ethanol are still the main by-products in the liquid phase, with ethanol being the most significant component. Ethanol is formed by ethylene glycol dehydration at the catalyst surface followed by hydrogenation [50]. The carbon yield towards liquid products was relatively low, with only between 3 % and 6 % of the carbon present in the feedstock converted to liquid products (Fig. 7 [d]).

All catalysts presented in this study follow similar trends in the selectivity towards gas and liquid phase products, suggesting that the addition of Mn and heteroatoms on the surface of the catalyst support only have minor impact on the product distribution. However, enhancement in the catalytic activity is observed when Mn and N are present in the Pt-based catalysts. These similarities in the composition of the by-products show that APR of ethylene glycol over CNF-supported catalysts correlates with the reaction pathways published previously, initially reported by Dumesic et al. favoring C-C bond cleavage over C-O bond cleavage, resulting in high H_2 selectivities [1,50–52] as presented

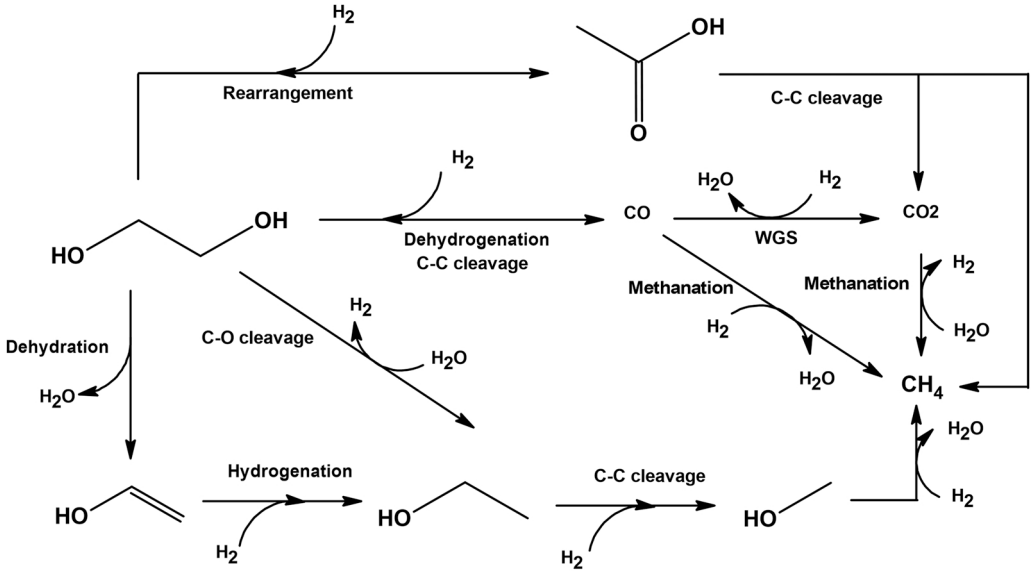

Fig. 8. Reaction scheme for aqueous phase reforming of ethylene glycol.

in the following reaction scheme (Fig. 8).

3.4. Characterization of spent catalysts

To understand the possible role of deactivation due to metal oxidation, leaching and sintering, the spent catalysts were analyzed after being exposed to APR. In continuous operation, significant metal leaching was detected after 20 h of reaction for the Mn-containing samples (Table S7). For PtMn CNF-HT, 97.1 ± 0.1 % of the Mn was lost during APR, while for PtMn N-CNF, the Mn leaching was estimated to be slightly lower at 89.0 ± 0.1 %. This indicates that functionalizing the carbon surface with N-containing groups may help stabilize some of the Mn present in the catalyst. In the case of Pt, no significant leaching was detected (<0.01 %) (Table S7).

In the current study, STEM-EDX analysis revealed the presence of Pt and Mn in the catalysts and evidence of the proximity between Mn and Pt in the reduced catalysts (Figs. S8 and S9).

Furthermore, from the STEM images in Fig. 4, the particles seem homogeneously distributed on the carbon support for all the samples, and no significant changes are observed for the spent catalysts. However, a slight decrease in the dispersion after reaction (Table 5) is observed, suggesting minor sintering of the metal particles caused by the harsh hydrothermal conditions in APR.

XPS characterization of the spent N-doped bimetallic catalyst after APR was carried out, and the results are presented in Figs. 3 and 4. The N 1 s spectrum of the spent PtMn N-CNF (Fig. 3 [d]) shows similar fractions of oxidized, quaternary, pyrrolic, and pyridinic nitrogen functional groups with an overall N content of 1.2 %at. The N content is comparable to the catalyst after reduction, indicating that the nitrogen species located on the surface of the CNF are sufficiently stable to withstand the hydrothermal conditions of APR.

Despite the substantial loss of Mn during the reaction (Fig. S9) the catalytic activity of the samples is maintained as can be seen in Fig. 7 and from the Pt 4 $f_{7/2}$ spectra of the spent bimetallic catalyst after APR (Table 4) it still can be seen a shift to higher binding energies of approximately 1.0 eV for Pt when compared to the monometallic catalyst. Therefore, it seems that the leached Mn species from the catalyst surface have a negligible impact on catalyst activity. Bossola *et al.* [9] observed similar results, where only 5 % of the Mn was retained on the catalyst after APR. It was suggested that Pt was alloyed with the small amount of Mn still present in the sample, generating a promoting effect. The minor fraction of Mn in the catalyst positively impacts the catalytic activity toward H_2 production. Thus, it can be considered that the remaining Pt particles expose a larger fraction of low coordination surface atoms after Mn leaching. These low coordination surface atoms can be preferential sites for aqueous phase reforming of ethylene glycol.

4. Conclusions

The activity, selectivity, and stability of Pt-based catalysts for hydrogen production by APR of ethylene glycol were evaluated, initially by screening the catalyst in a batch setup, followed by further experiments in continuous flow conditions. It is observed that the activity of the catalysts was influenced by the nitrogen contained in the surface of the CNF support and promotion with manganese. In this context, it was demonstrated that bimetallic catalysts such as PtMn supported on N-doped carbon nanofibers are active and selective catalysts in aqueous phase reforming of ethylene glycol, with H_2 site time yield of 15.8 min^{-1} at 225 °C and 30 bar pressure. The enhancement in catalytic activity could be attributed to metal-support interactions between PtMn and N-doped carbon nanofibers, decreasing the electron density on Pt and promoting H_2 formation. The addition of Mn to the Pt-based catalysts further decreased the electron density of Pt by metal-metal interaction and enhancing the catalytic activity.

After 20 h of continuous-flow APR, up to 97 ± 0.1 % of Mn was lost to leaching. N-doping of the support was able to slightly suppress the metal leaching, with 89 ± 0.1 % of Mn lost. However, it was found that Mn leaching does not negatively affect the catalytic activity, indicating that a small fraction of Mn is sufficient to improve the catalytic activity of Pt.

Table 5
Metal dispersion and average Pt particle size by CO chemisorption of reduced and spent catalyst.

Catalyst	Pt dispersion (+/- 1 %)		Pt particle size (nm)	
	Reduced	Spent	Reduced	Spent
Pt CNF-HT	50	44	2	3
Pt N-CNF	40	35	3	3
PtMn CNF-HT	34	35	3	3
PtMn N-CNF	35	31	3	4

CRediT authorship contribution statement

Monica Pazos Urrea: Conceptualization, Methodology, Validation, Formal analysis, Investigation, Writing – original draft, Writing – review & editing, Visualization. **Felix Herold:** Conceptualization, Validation, Formal analysis, Investigation, Resources, Writing – review & editing, Visualization. **De Chen:** Conceptualization, Validation, Supervision. **Magnus Rønning**: Conceptualization, Validation, Writing – review & editing, Supervision, Project administration, Funding acquisition.

Declaration of Competing Interest

The authors declare that they have no known competing financial interests or personal relationships that could have appeared to influence the work reported in this paper.

Data availability

Data will be made available on request.

Acknowledgements

This work was financially supported by the European Union's Horizon 2020 Research and Innovation Program under the Marie Skłodowska-Curie Actions−Innovative Training Networks (MSCA-ITN) BIKE project, Grant Agreement 813748. FH acknowledges a fellowship within the Walter-Benjamin-program of the Deutsche Forschungsgemeinschaft (DFG, German Research Foundation, project number 471263729). The Research Council of Norway is acknowledged for the support to the Norwegian Micro- and Nano-Fabrication Facility, NorFab (project number 295864), and the national infrastructure NorBioLab (project number 270038). Trung Dung Tran at Johnson Matthey is acknowledged for performing the TEM study.

Appendix A. Supporting information

Additional results of XPS, STEM, catalytic testing and detailed experimental procedures concerning XPS. Supplementary data associated with this article can be found in the online version at doi:10.1016/j.cattod.2023.114066.

References

[1] R.D. Cortright, R.R. Davda, J.A. Dumesic, Nature 418 (2002) 964–967.
[2] K. Oshiro, S. Fujimori, Appl. Energy 313 (2022), 118803.
[3] B. Roy, K. Loganathan, H.N. Pham, A.K. Datye, C.A. Leclerc, Int. J. Hydrog. Energy 35 (2010) 11700–11708.
[4] A.V.-H. Soares, G. Perez, F.B. Passos, Appl. Catal. B Environ. 185 (2016) 77–87.
[5] A.O. Menezes, M.T. Rodrigues, A. Zimmaro, L.E.P. Borges, M.A. Fraga, Renew. Energy 36 (2011) 595–599.
[6] J.W. Shabaker, G.W. Huber, R.R. Davda, R.D. Cortright, J.A. Dumesic, Catal. Lett. 88 (2003) 1–8.

[7] T. van Haasterecht, C.C.I. Ludding, K.P. de Jong, J.H. Bitter, J. Energy Chem. 22 (2013) 257–269.
[8] M.-C. Kim, T.-W. Kim, H.J. Kim, C.-U. Kim, J.W. Bae, Renew. Energy 95 (2016) 396–403.
[9] F. Bossola, X.I. Pereira-Hernández, C. Evangelisti, Y. Wang, V. Dal Santo, J. Catal. 349 (2017) 75–83.
[10] A. Volynkin, M. Rønning, E.A. Blekkan, Top. Catal. 58 (2015) 854–865.
[11] H.-D. Kim, H.J. Park, T.-W. Kim, K.-E. Jeong, H.-J. Chae, S.-Y. Jeong, C.-H. Lee, C.-U. Kim, Int. J. Hydrog. Energy 37 (2012) 8310–8317.
[12] J. Gan, Z. Huang, W. Luo, W. Chen, Y. Cao, G. Qian, X. Zhou, X. Duan, J. Energy Chem. 52 (2021) 33–40.
[13] R. Zheng, Y. Zhao, H. Liu, C. Liang, G. Cheng, Carbon 44 (2006) 742–746.
[14] I. Kvande, D. Chen, T.-J. Zhao, I.M. Skoe, J.C. Walmsley, M. Rønning, Top. Catal. 52 (2009) 664–674.
[15] W. Chen, S. Chen, G. Qian, L. Song, D. Chen, X. Zhou, X. Duan, J. Catal. 389 (2020) 492–501.
[16] C.F. Sanz-Navarro, P.-O. Åstrand, D. Chen, M. Rønning, A.C.T. van Duin, T. Jacob, W.A. Goddard, J. Phys. Chem. A 112 (2008) 1392–1402.
[17] G. Pipitone, G. Zoppi, R. Pirone, S. Bensaid, Int. J. Hydrog. Energy (2021). S0360319921037848.
[18] M. El Doukkali, A. Iriondo, J.F. Cambra, I. Gandarias, L. Jalowiecki-Duhamel, F. Dumeignil, P.L. Arias, Appl. Catal. Gen. 472 (2014) 80–91.
[19] D.L. King, L. Zhang, G. Xia, A.M. Karim, D.J. Heldebrant, X. Wang, T. Peterson, Y. Wang, Appl. Catal. B Environ. 99 (2010) 206–213.
[20] X. Wang, N. Li, L.D. Pfefferle, G.L. Haller, Catal. Today 146 (2009) 160–165.
[21] G.W. Huber, J.W. Shabaker, S.T. Evans, J.A. Dumesic, Appl. Catal. B Environ. 62 (2006) 226–235.
[22] L.I. Godina, A.V. Kirilin, A.V. Tokarev, I.L. Simakova, D.Y. Murzin, Ind. Eng. Chem. Res. 57 (2018) 2050–2067.
[23] P. Gogoi, N. Kanna, P. Begum, R.C. Deka, S.C.V. V, T. Raja, ACS Catal. 10 (2020) 2489–2507.
[24] K. Jiang, X.-Y. Ma, S. Back, J. Zhao, F. Jiang, X. Qin, J. Zhang, W.-B. Cai, CCS Chem. 3 (2021) 241–251.
[25] A. García-Baldoví, L. Peng, A. Santiago-Portillo, A.M. Asiri, A. Primo, H. García, ACS Appl. Energy Mater. 5 (2022) 9173–9180.
[26] Z. Zheng, Y. Fang, J. Yang, L. Ma, Q. Meng, X. Lin, Y. Liu, Q. Zhang, T. Wang, Int. J. Hydrog. Energy 47 (2022) 950–961.
[27] D. Chen, K.O. Christensen, E. Ochoa-Fernández, Z. Yu, B. Tøtdal, N. Latorre, A. Monzón, A. Holmen, J. Catal. 229 (2005) 82–96.
[28] S. Brunauer, P.H. Emmett, E. Teller, J. Am. Chem. Soc. 60 (1938) 309–319.
[29] M. Fadoni, L. Lucarelli, Stud. Surf. Sci. Catal. 120 (1999) 177–225.
[30] S. Gražulis, D. Chateigner, R.T. Downs, A.F.T. Yokochi, M. Quirós, L. Lutterotti, E. Manakova, J. Butkus, P. Moeck, A. Le Bail, J. Appl. Crystallogr. 42 (2009) 726–729.
[31] C.F. Holder, R.E. Schaak, ACS Nano 13 (2019) 7359–7365.
[32] D.A. Shirley, Phys. Rev. B 5 (1972) 4709–4714.
[33] S.K. Jain, E.M. Crabb, L.E. Smart, D. Thompsett, A.M. Steele, Appl. Catal. B Environ. 89 (2009) 349–355.
[34] N. Muthuswamy, J.L.G. de la Fuente, P. Ochal, R. Giri, S. Raaen, S. Sunde, M. Rønning, D. Chen, Phys. Chem. Chem. Phys. 15 (2013) 3803–3813.
[35] C. Prado-Burguete, A. Linares-Solano, F. Rodríguez-Reinoso, C.S.-M. de Lecea, J. Catal. 115 (1989) 98–106.
[36] K. Friedel Ortega, R. Arrigo, B. Frank, R. Schlögl, A. Trunschke, Chem. Mater. 28 (2016) 6826–6839.
[37] M. Zhao, Y. Xia, J.P. Lewis, R. Zhang, J. Appl. Phys. 94 (2003) 2398–2402.
[38] T. Kondo, S. Casolo, T. Suzuki, T. Shikano, M. Sakurai, Y. Harada, M. Saito, M. Oshima, M.I. Trioni, G.F. Tantardini, J. Nakamura, Phys. Rev. B 86 (2012), 035436.
[39] L. Jia, D.A. Bulushev, O.Yu Podyacheva, A.I. Boronin, L.S. Kibis, E.Yu Gerasimov, S. Beloshapkin, I.A. Seryak, Z.R. Ismagilov, J.R.H. Ross, J. Catal. 307 (2013) 94–102.
[40] L.P.L. Gonçalves, M. Meledina, A. Meledin, D.Y. Petrovykh, J.P.S. Sousa, O.S.G. P. Soares, Y.V. Kolen'ko, M.F.R. Pereira, Carbon 195 (2022) 35–43.
[41] O.Yu Podyacheva, A.S. Lisitsyn, L.S. Kibis, A.I. Stadnichenko, A.I. Boronin, E. M. Slavinskaya, O.A. Stonkus, S.A. Yashnik, Z.R. Ismagilov, Catal. Today 301 (2018) 125–133.
[42] J. Zhao, C. Fu, K. Ye, Z. Liang, F. Jiang, S. Shen, X. Zhao, L. Ma, Z. Shadike, X. Wang, J. Zhang, K. Jiang, Nat. Commun. 13 (2022) 685.
[43] Y.-H. Li, T.-H. Hung, C.-W. Chen, Carbon 47 (2009) 850–855.
[44] Z. Wu, B.C. Bukowski, Z. Li, C. Milligan, L. Zhou, T. Ma, Y. Wu, Y. Ren, F. H. Ribeiro, W.N. Delgass, J. Greeley, G. Zhang, J.T. Miller, J. Am. Chem. Soc. 140 (2018) 14870–14877.
[45] L. Calvillo, M. Gangeri, S. Perathoner, G. Centi, R. Moliner, M.J. Lázaro, J. Power, Sources 192 (2009) 144–150.
[46] D.A. Bulushev, M. Zacharska, A.S. Lisitsyn, O.Yu Podyacheva, F.S. Hage, Q. M. Ramasse, U. Bangert, L.G. Bulusheva, ACS Catal. 6 (2016) 3442–3451.
[47] T. Maiyalagan, B. Viswanathan, U.V. Varadaraju, Electrochem. Commun. 7 (2005) 905–912.
[48] P.J. Dietrich, F.G. Sollberger, M.C. Akatay, E.A. Stach, W.N. Delgass, J.T. Miller, F. H. Ribeiro, Appl. Catal. B Environ. 156–157 (2014) 236–248.
[49] Z. Wei, A. Karim, Y. Li, Y. Wang, ACS Catal. 5 (2015) 7312–7320.
[50] J.W. Shabaker, J.A. Dumesic, Ind. Eng. Chem. Res. 43 (2004) 3105–3112.
[51] R.R. Davda, J.W. Shabaker, G.W. Huber, R.D. Cortright, J.A. Dumesic, Appl. Catal. B Environ. 56 (2005) 171–186.
[52] D.J.M. de Vlieger, B.L. Mojet, L. Lefferts, K. Seshan, J. Catal. 292 (2012) 239–245.